Nano Research 2017, 10(8): 2626–2632
DOI 10.1007/s12274-017-1465-y
Research Article
ISSN 1998-0124
CN 11-5974/O4

Rapid and multimodal *in vivo* bioimaging of cancer cells through *in situ* biosynthesis of Zn&Fe nanoclusters

Tianyu Du[1,§], Chunqiu Zhao[1,§], Fawad ur Rehman[1], Lanmei Lai[1], Xiaoqi Li[2], Yi Sun[3], Shouhua Luo[3], Hui Jiang[1], Matthias Selke[4], and Xuemei Wang[1] (✉)

[1] *State Key Laboratory of Bioelectronics (Chien-Shiung Wu Lab), School of Biological Science and Medical Engineering, Southeast University, Nanjing 210096, China*
[2] *Nanjing Foreign Language School, Nanjing 210096, China*
[3] *Laboratory of the signal and image processing, School of Biological Science and Medical Engineering, Southeast University, Nanjing 210096, China*
[4] *Department of Chemistry and Biochemistry, California State University, Los Angeles, CA 90032, USA*
[§] *These authors contributed equally to this work.*

Received: 25 September 2016
Revised: 30 December 2016
Accepted: 2 January 2017

KEYWORDS
multimodal imaging, biosynthesized, Zn&Fe oxide nanoclusters, cancer diagnosis

ABSTRACT

Early diagnosis remains highly important for efficient cancer treatment, and hence, there is significant interest in the development of effective imaging strategies. This work reports a new multimodal bioimaging method for accurate and rapid diagnosis of cancer cells by introducing aqueous Fe^{2+} and Zn^{2+} ions into cancer cells (i.e., HeLa, U87, and HepG2 cancer cells). We found that the biocompatible metal ions Fe^{2+} and Zn^{2+} forced the cancer cells to spontaneously synthesize fluorescent ZnO nanoclusters and magnetic Fe_3O_4 nanoclusters. These clusters could then be used for multimodal cancer imaging by combining fluorescence imaging with magnetic resonance imaging and computed tomography imaging. Meanwhile, for normal cells (i.e., L02) and tissues, neither fluorescence nor any other obvious difference could be detected between pre- and post-injection. This multimodal bioimaging strategy based on the *in situ* biosynthesized Zn&Fe oxide nanoclusters might therefore be useful for early cancer diagnosis and therapy.

1 Introduction

Early cancer diagnosis remains a critical strategy for reducing cancer mortality and improving the cure rate [1, 2]. Among the diagnostic methods, biomedical imaging technology is considered a highly promising strategy. In this respect, fluorescence bioimaging, magnetic resonance imaging (MRI), X-ray computed tomography (CT), ultrasound imaging [3–8], etc. have gradually become primary diagnosis techniques. Fluorescence imaging could be efficiently utilized for precise and real-time monitoring of tumors due

Address correspondence to xuewang@seu.edu.cn

to improved fluorescence imaging technology and nanoscaled probes including noble metal nanoclusters and quantum dots [2–5, 9–11]. Our recent studies also demonstrated that some biocompatible metal ions, such as Au (III), Ag (I), and Pt (IV), can be readily reduced by excess reduced monomeric glutathione (GSH) or triphosphopyridine nucleotide and nicotinamide adenine dinucleotide (NAD(P)H) to form fluorescent nanoclusters in cancer cells, leading to *in situ* fluorescent bioimaging of cancers [12–14].

One drawback of fluorescence bioimaging is the limited penetration depth for deep-seated neoplasms, and the autofluorescence of tissues may also interfere with the detection sensitivity. In the latter case, MRI and/or CT imaging could provide an effective alternative for the rapid and accurate diagnosis of cancers [15–17]. Combining the high penetration depth of MRI and the anatomical information from CT, multimodal bioimaging can be achieved if effective fluorescence enhancement can be introduced. In MRI, the use of imaging agents will significantly improve the quality of the image [18–21]. Commonly, imaging agents for MRI can be classified as T_1 and T_2 imaging agents by their different action mechanisms. Superparamagnetic Fe_3O_4 nanoparticles, which can decrease the transverse relaxation time of H_2O, have been widely used as a negative contrast T_2 imaging agent in clinical diagnosis [22–26]. Based on these observations, in this contribution, we have explored a new multimodal bioimaging strategy via biosynthesized nanoclusters of fluorescent ZnO and superparamagnetic Fe oxides. Our observations demonstrate that when zinc gluconate and $FeCl_2$ solution were cultured with cells or intravenously injected into xenografted nude mice, the ions were readily reduced, and fluorescent ZnO nanoclusters and magnetic Fe_3O_4 nanoclusters were spontaneously biosynthesized. These nanoclusters can be used for multimodal cancer imaging through a combination of bright fluorescence imaging with MRI and CT imaging (Scheme 1).

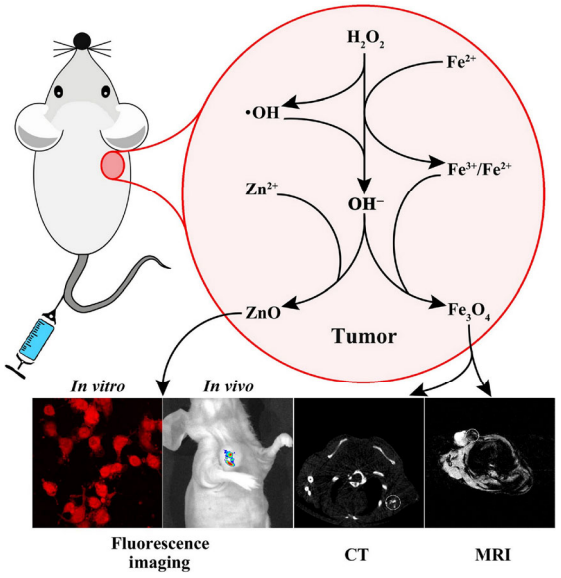

Scheme 1 *In situ* biosynthesis of Zn&Fe oxide nanoclusters and subsequent *in vivo* multimodal bioimaging of cancer cells.

2 Experimental

HepG2, HeLa, U87, and L02 cells were cultured in Dulbecco's modified Eagle medium (DMEM) under a 5% CO_2 atmosphere at 37 °C. When the concentration of cells reached approximately 100,000 per well, 300 μM $Zn(C_6H_{11}O_7)_2$ and 300 μM $FeCl_2$ were added into the DMEM within six-well plates (for control assay, only phosphate buffer saline (PBS) was used). After 48 h of incubation, the cells were washed by PBS (5 mL × 3) and then observed under a laser confocal fluorescence microscope (Leica TCS SP2) with an excitation wavelength of 440 nm and emission wavelength of 650 nm.

Subcutaneous tumor models were generated by the subcutaneous inoculation (0.10 mL volume containing 5×10^7 cells/mL media) of Hela or HepG2 cells in the right side of the oxter using a 1-mL syringe with a 25G needle. Tumor growth was monitored until a palpable size of approximately 1.0 cm in length was reached in any direction. After anesthetizing with 5% isoflurane (O_2-balanced), a 100-μL solution that contained 5 mM $Zn(C_6H_{11}O_7)_2$ or/and 8 mM $FeCl_2$ was injected into the tail vein or subcutaneously. Then the bioimaging fluorescence was monitored in real-time by the PerkinElmer® *in vivo* imaging system (IVIS Lumina XRMS Series III) with an excitation wavelength of 440 nm and emission wavelength of 670 nm in a 24-h period. T_2-weighted MRI imaging was conducted on a 7.0 T Micro-MR (PharmaScan 70/17 Brucker).

The nanoclusters in tumors were extracted via a freeze-thaw method [6]. Energy-dispersive X-ray

spectroscopy (EDS) was performed using a Zeiss Ultra Plus scanning electron microscope. X-ray photoelectron spectroscopy (XPS) was performed on a PHI Quantera II with Al Kα X-ray (h = 1,486.6 eV) radiation operated at 135 W to investigate the surface atomic concentrations and the oxidation state distribution of the elements in the samples. All binding energies (BE) were referenced to the adventitious C1s at 284.4 eV. UV–Vis absorption spectroscopy and fluorescence spectra were recorded on Thermo Scientific BioMate-3S and PerkinElmer LS-55 spectrophotometer, respectively. The micromorphology of the nanoclusters was examined on a JEOL JEM-2100 transmission electron microscope (TEM). CT imaging was performed on a Hiscan-M1000 CT instrument.

3 Results and discussion

Initially, the fluorescent bioimaging efficiency of Zn^{2+} and Fe^{2+} has been explored by *in vitro* studies with confocal fluorescence microscopy using the same method as that described in our previous report [27], where cancer cells including HeLa, U87, and HepG2 and normal or non-cancerous cells like L02 were respectively incubated with 300 μM $Zn(C_6H_{11}O_7)_2$ or/and $FeCl_2$ for 24 h, while in control experiments only DMEM was incubated with the above cells. As shown in Fig. 1(a), after 24 h of incubation, no detectable fluorescence was observed from the control group and the Fe group (i.e., with $FeCl_2$ alone) for all cells. This implies that Fe oxides alone cannot contribute to the intracellular fluorescence signal. In contrast, in the presence of the $Zn(C_6H_{11}O_7)_2$ complex, bright fluorescence was clearly observed from cancer cells such as HeLa, U87, and HepG2. Furthermore, comparing the intracellular fluorescence intensity of the Zn group (i.e., with $Zn(C_6H_{11}O_7)_2$ alone) with that of the Fe&Zn groups (i.e., with $Zn(C_6H_{11}O_7)_2$ and $FeCl_2$), we found that the addition of Fe^{2+} enhanced the fluorescence intensity. The experiments in which only Fe^{2+} was present (from $FeCl_2$) indicated that the presence of iron oxides alone did not seem to affect intracellular fluorescence. However, it may be possible that the formation of iron oxides does indeed promote the ZnO product to a certain degree. Another notable aspect is that the L02 cells showed little or no fluorescence under all of the conditions. This observation suggests that the synthesis of fluorescent ZnO nanoclusters only occurred in the cancer cells, thereby allowing the rapid discrimination between

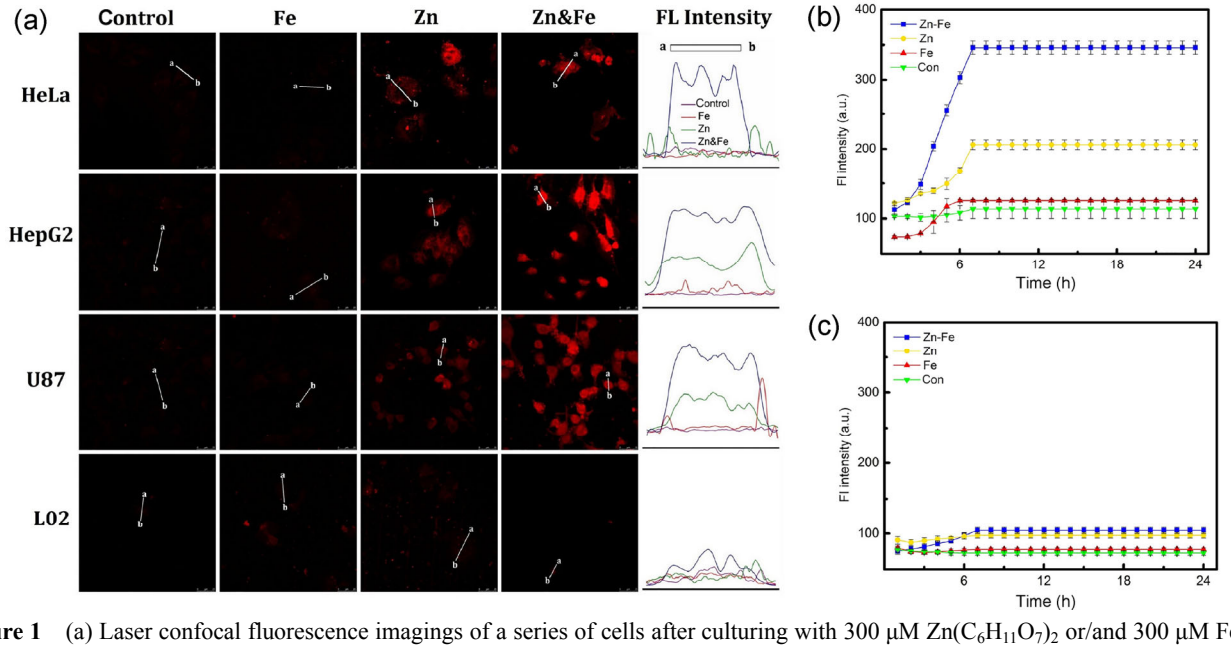

Figure 1 (a) Laser confocal fluorescence imagings of a series of cells after culturing with 300 μM $Zn(C_6H_{11}O_7)_2$ or/and 300 μM $FeCl_2$ for 24 h. For the control group, only DMEM was used. Figures on the right show the relative fluorescence intensity of the cells along the cross-section. Purple line, red line, green line, and blue line represent control, Fe, Zn, and Zn&Fe groups, respectively. Real-time monitoring of the fluorescence intensity of (b) HepG2 and (c) L02 was performed using high-content cell analysis.

non-cancerous and cancer cells. The same results were also observed by high-content cell analysis (Figs. 1(b) and 1(c)). For HepG2 cells, fluorescence emerged and increased with time in the initial 6 h while they were treated with Zn^{2+}. No obvious fluorescence was detected in the control group (Movies S1 and S2 in the Electronic Supplementary Material (ESM)).

As described above, our results established the feasibility of *in vivo* detection. We then applied this methodology for the following *in vivo* tumor bioimaging study with a xenografted nude mice model. We intravenously injected 0.1 mL of a solution containing 5 mM $Zn(C_6H_{11}O_7)_2$ or/and 5 mM $FeCl_2$ (for the control group, only PBS was used) through the tails into the tumor of xenografted nude mice models of HepG2. As shown in Fig. 2, rapid *in vivo* fluorescence tumor imaging was realized with an excitation wavelength of 440 nm and an emission wavelength of 670 nm. It is evident from Fig. 2 that bright fluorescence could be observed in the tumor sites for both the Zn and the Zn&Fe group 4 h after intravenous ion injection. The fluorescence intensity continued to increase with time and reached a maximum after approximately 18 h (Fig. 2(b)). Furthermore, it is noteworthy that under the same experimental conditions, the Zn&Fe group always showed higher fluorescence intensity in the tumor sites when compared with that of the Zn group at the same sampling point. No detectable fluorescence appeared in the Fe and control groups within the entire period (Fig. S1 in the ESM). This result is in agreement with the *in vitro* studies. In addition, *ex vivo* fluorescence studies confirmed (Fig. S2 in the ESM) that the fluorescence materials were mostly located in the tumors, while only weak fluorescence was detected in the liver and no fluorescence was observed in any other organ. These phenomena indicated that self-bioimaging for the Zn&Fe group could be established for *in vivo* tumor imaging, and the introduction of Fe could efficiently enhance the fluorescence intensity. The liver and kidney are the main organs that excrete metal clusters, and the weak fluorescence in these organs confirmed that the biosynthesized clusters can remain *in vivo* for at least 24 h, which could be another advantage of this bioimaging technology.

In comparison, the results of T_2-weighted MRI and CT are shown in Figs. 2(c) and 2(d), and Fig. S3 in the ESM. In the Zn&Fe group, 24 h after intravenous injection, the tumor region (indicated by white circle) became dark (for MRI) or bright (for CT) whereas no obvious differences were observed in the control group. The T_2-weighted MRI signal was always due

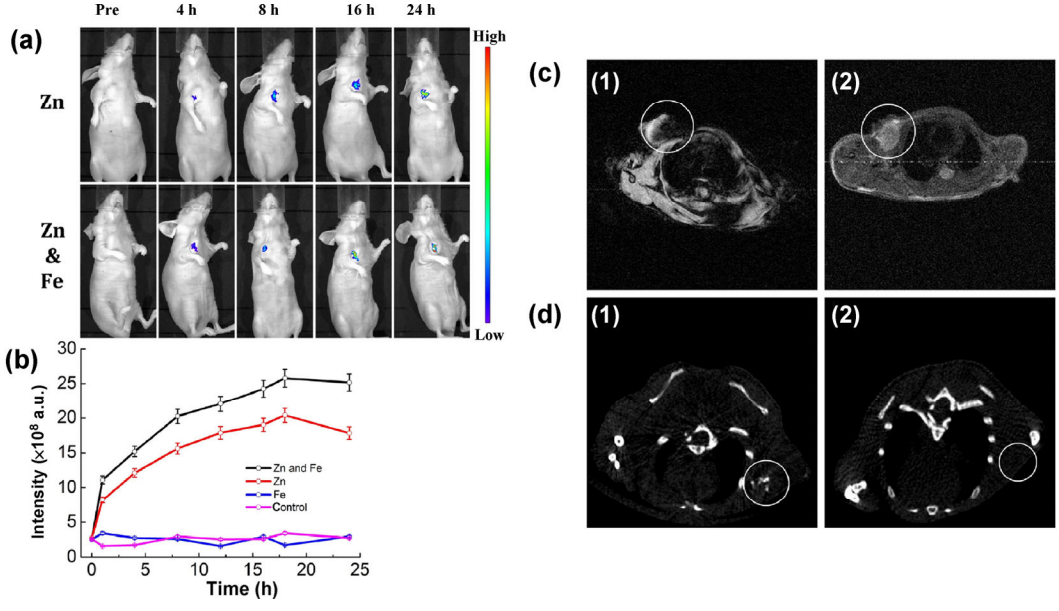

Figure 2 (a) *In vivo* fluorescence on HepG2-xenografted tumor mice after injecting 5 mM $Zn(C_6H_{11}O_7)_2$ and 5 mM $FeCl_2$ (if used) at a series of time points and (b) quantitative analysis of fluorescence intensity. (c) T_2-weighted MRI imaging and (d) CT imaging of mice in (1) Zn&Fe and (2) control group (24 h after injecting, the tumor is indicated by white circle).

to superparamagnetic iron oxides, which, in this work, was most probably formed from the Fe^{2+} precursor. Furthermore, we observed that this Fe species could readily act as a CT contrast agent. It is evident that compared to the conventional imaging agents that are usually synthesized under high temperature and high pressure, this *in situ* bioimaging method can achieve multimodal imaging via the simple introduction of Zn^{2+} and Fe^{2+} ions, where the ZnO and Fe_3O_4 clusters can be readily biosynthesized under mild conditions by utilizing the difference in the redox environment between cancerous cells and normal cells.

On the basis of the above studies, the elements in tumor extracts were further investigated by EDS analysis (Fig. S3 in the ESM). The abnormally high content of Fe and Zn revealed that these metal species have not yet been completely excreted by tumor tissues. Figures 3(a) and 3(b) show the XPS results of the biosynthesized metal oxides, where the signal peaks at 1,021.5 and 1,045.1 eV are attributed to Zn (II), while for the Fe ions, after deconvoluting the XPS band from 700 to 730 eV, we found that both Fe(II) and Fe(III) co-existed in the tumor tissue samples. From the integrated peak area, we found that the +2 valence state of Fe accounts for 53.2% of total iron. Figures 3(f) and 3(g) depict the particle size of the biosynthesized metal oxides via high-resolution TEM. To distinguish Zn and Fe oxides in this process, $FeCl_2$ solution and zinc gluconate solution were injected intravenously into two groups of xenografted nude mice models of HepG2, followed by extraction of the biosynthesized samples that were characterized by TEM. It can be seen that the biosynthesized ZnO and Fe_3O_4 nanoparticles have the same size, 5 nm, and the residual tissues cap the nanoparticles and make them blurry. The interplanar spacing between them is approximately 0.162 and 0.260 nm, respectively, corresponding to the (110) plane of ZnO and (311) plane of Fe_3O_4. In this experiment, only Fe^{2+} was used as a precursor and thus, the appearance of Fe^{3+} should result from the partial oxidation of Fe^{2+} in the tumor tissues. For cancer cells, it is already known that the concentrations of reactive oxygen species (ROS) such as H_2O_2 are much higher than those in normal cells [28, 29]. The existence of ROS affects the Fe^{2+} and brings it to a higher valence state. Figure 3(e) and Fig. S3 in the ESM show the impact of H_2O_2 on Fe^{2+}. $FeCl_2$ solutions in PBS (50–3,000 μM) were mixed with different

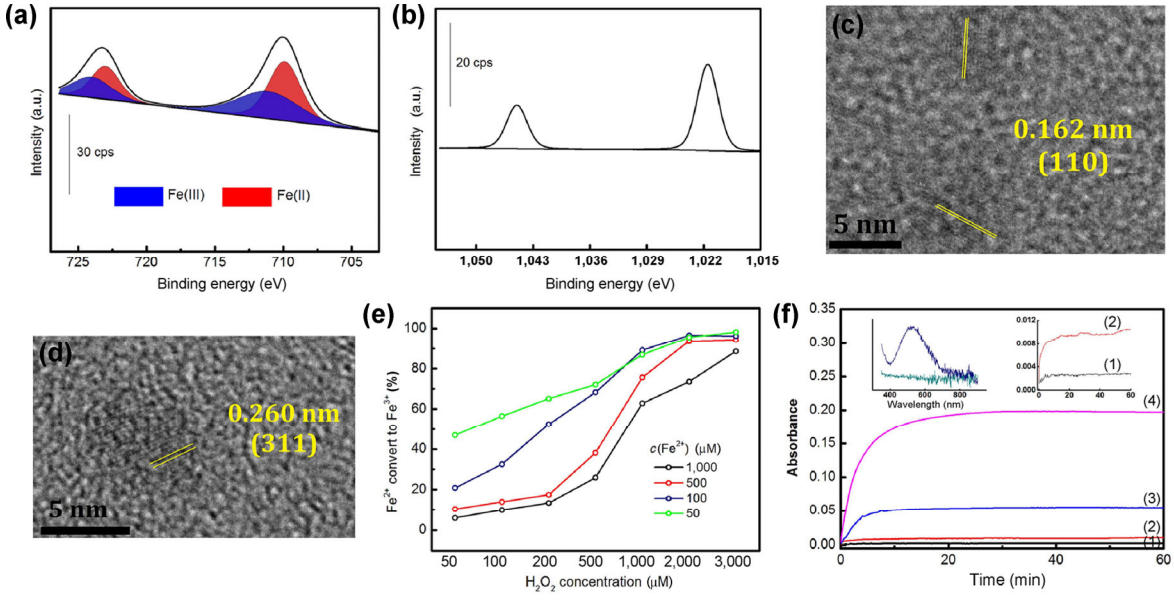

Figure 3 (a) Fe2p and (b) Zn2p XPS spectra of the *in vivo* extract. High-resolution TEM images of the *in vivo* extracted (c) ZnO and (d) Fe_3O_4 nanoclusters. (e) Oxidation of Fe^{2+} by H_2O_2 and formation of Fe^{3+} under different concentrations. (f) Formation of ·OH from H_2O_2 under catalysis of Fe^{2+} indicated by salicylic acid at an absorbance at λ = 510 nm. The reaction concentrations are (1) 50 μM H_2O_2 + 50 μM Fe^{2+}, (2) 100 μM H_2O_2 + 50 μM Fe^{2+}, (3) 200 μM H_2O_2 + 50 μM Fe^{2+}, and (4) 500 μM H_2O_2 + 50 μM Fe^{2+}.

concentrations of H_2O_2 (50–3,000 μM) for 10 min, followed by spectrophotometric determination of the Fe^{2+} concentration at λ = 511 nm after coordinating the iron with 1,10-phenanthroline. With a higher H_2O_2/Fe^{2+} ratio or lower Fe^{2+} concentration, the Fe^{2+} will obviously be converted to Fe^{3+}. This observation provides reliable evidence for the appearance of Fe^{3+}. This further illustrates the relationship between Fe^{2+} oxidization to Fe^{3+} and hydroxyl radicals, formed from H_2O_2 via the Fenton reaction. Figure 3(e) shows the formation of ·OH, indicated by its reaction with salicylic acid in PBS [18]. The as-formed products exhibited absorption at 510 nm (Fig. 3(f) inset), which could be expressed as a function of time under a series of concentrations. It can be seen that most ·OH appears to be generated in the initial 10 min after the addition of H_2O_2 to Fe^{2+}, and the yield of ·OH increased with H_2O_2 concentration. The fluorescence spectrum of the biosynthesized ZnO nanoclusters is displayed in Fig. S3 (in the ESM), where the excitation peak at 431 nm and emission peak at 650 nm are attributed to ZnO nanoparticles [30]. Considering that cells always maintain a constant intracellular fluid pH, and combining the observations described above, the introduction of Zn^{2+} and Fe^{2+} may result in such a pathway in cancer cells

$$Fe^{2+} + H_2O_2 \rightarrow Fe^{3+} + OH^- + \cdot OH \quad (1)$$

$$Fe^{2+} + \cdot OH \rightarrow Fe^{3+} + OH^- \quad (2)$$

$$Fe^{2+} + 2Fe^{3+} + 8OH^- \rightarrow Fe_3O_4 + 4H_2O \quad (3)$$

$$Zn^{2+} + 2OH^- \rightarrow ZnO + H_2O \quad (4)$$

4 Conclusions

In summary, in this study we have explored a novel *in vivo* multimodal bioimaging method for the early detection of tumors based on *in situ* biosynthesized Zn&Fe oxide nanoclusters. Our observations demonstrate that by introducing Zn^{2+} and Fe^{2+} ions via a single injection, fluorescent ZnO nanoclusters and superparamagnetic Fe_3O_4 nanoparticles can be spontaneously self-biosynthesized in tumor cells/tissues, which then contribute to the fluorescence and T_2-weighted MRI signal, respectively. The resultant Zn and Fe oxides most probably stem from excess ROS, such as H_2O_2 in cancer cells. More importantly, such a self-biosynthetic process is not found in normal cells or normal tissues. This could be a significant advantage of this *in situ* multimode bioimaging method to achieve the rapid and accurate diagnosis of tumors. The relatively non-toxic agents and simple operation make this a potentially useful method for early cancer detection.

Acknowledgements

This work is supported by the National High-tech R&D Program of China (No. 2015AA020502) and the National Natural Science Foundation of China (Nos. 81325011, 21327902 and 21175020). M. S. acknowledges support from the NSF-PREM program (No. DRM-1523588).

Electronic Supplementary Material: Supplementary material (*in vivo* fluorescence, CT and MRI images of control groups) is available in the online version of this article at http://dx.doi.org/10.1007/s12274-017-1465-y.

References

[1] Peto, J. Cancer epidemiology in the last century and the next decade. *Nature* **2001**, *411*, 390–395.

[2] Wang, C. S.; Li, J. Y.; Amatore, C.; Chen, Y.; Jiang, H.; Wang, X. M. Gold nanoclusters and graphene nanocomposites for drug delivery and imaging of cancer cells. *Angew. Chem., Int. Ed.* **2011**, *50*, 11644–11648.

[3] Qiu, J. J.; Xiao, Q. F.; Zheng, X. P.; Zhang, L. B.; Xing, H. Y.; Ni, D. L.; Liu, Y. Y.; Zhang, S. J.; Ren, Q. G.; Hua, Y. Q. et al. Single $W_{18}O_{49}$ nanowires: A multifunctional nanoplatform for computed tomography imaging and photothermal/photodynamic/radiation synergistic cancer therapy. *Nano Res.* **2015**, *8*, 3580–3590.

[4] Lee, N.; Choi, S. H.; Hyeon, T. Nano-sized CT contrast agents. *Adv. Mater.* **2013**, *25*, 2641–2660.

[5] Liu, T.; Wu, G. Y.; Cheng, J. J.; Lu, Q.; Yao, Y. J.; Liu, Z. J.; Zhu, D. C.; Zhou, J.; Xu, J. R.; Zhu, J. et al. Multifunctional lymph-targeted platform based on Mn@mSiO$_2$ nanocomposites: Combining PFOB for dual-mode imaging and DOX for cancer diagnose and treatment. *Nano Res.* **2016**, *9*, 473–489.

[6] Yu, J.; Hao, R.; Sheng, F. G.; Xu, L. L.; Li, G. J.; Hou, Y. L. Hollow manganese phosphate nanoparticles as smart multifunctional probes for cancer cell targeted magnetic resonance imaging and drug delivery. *Nano Res.* **2012**, *5*, 679–694.

[7] Yang, Z. Z.; Ding, X. G.; Jiang, J. Facile synthesis of magnetic-plasmonic nanocomposites as T_1 MRI contrast enhancing and photothermal therapeutic agents. *Nano Res.* **2016**, *9*, 787–799.

[8] Shin, T. H.; Choi, J. S.; Yun, S.; Kim, I. S.; Song, H. T.; Kim, Y.; Park, K. I.; Cheon, J. T_1 and T_2 dual-mode MRI contrast agent for enhancing accuracy by engineered nanomaterials. *ACS Nano* **2014**, *8*, 3393–3401.

[9] Lehnert, B. E.; Goodwin, E. H.; Deshpande, A. Extracellular factor(s) following exposure to α particles can cause sister chromatid exchanges in normal human cells. *Cancer Res.* **1997**, *57*, 2164–2171.

[10] Taylor, D.; Hazenberg, J. G.; Lee, T. C. Living with cracks: Damage and repair in human bone. *Nat. Mater.* **2007**, *6*, 263–268.

[11] Cohen-Hoshen, E.; Bryant, G. W.; Pinkas, I.; Sperling, J.; Bar-Joseph, I. Exciton-plasmon interactions in quantum dot-gold nanoparticle structures. *Nano Lett.* **2012**, *12*, 4260–4264.

[12] Wang, J. L.; Zhang, G.; Li, Q. W.; Jiang, H.; Liu, C. Y.; Amatore, C.; Wang, X. M. *In vivo* self-bio-imaging of tumors through *in situ* biosynthesized fluorescent gold nanoclusters. *Sci. Rep.* **2013**, *3*, 1157.

[13] Gao, S. P.; Chen, D. H.; Li, Q. W.; Ye, J.; Jiang, H.; Amatore, C.; Wang, X. M. Near-infrared fluorescence imaging of cancer cells and tumors through specific biosynthesis of silver nanoclusters. *Sci. Rep.* **2014**, *4*, 4384.

[14] Chen, D. H.; Zhao, C. Q.; Ye, J.; Li, Q. W.; Liu, X. L.; Su, M. N.; Jiang, H.; Amatore, C.; Selke, M.; Wang, X. M. *In situ* biosynthesis of fluorescent platinum nanoclusters: Toward self-bioimaging-guided cancer theranostics. *ACS Appl. Mater. Interfaces* **2015**, *7*, 18163–18169.

[15] Chen, Q.; Li, K. G.; Wen, S. H.; Liu, H.; Peng, C.; Cai, H. D.; Shen, M. W.; Zhang, G. X.; Shi, X. Y. Targeted CT/MR dual mode imaging of tumors using multifunctional dendrimer-entrapped gold nanoparticles. *Biomaterials* **2013**, *34*, 5200–5209.

[16] Chen, Y.; Chen, H. R.; Shi, J. L. *In vivo* bio-safety evaluations and diagnostic/therapeutic applications of chemically designed mesoporous silica nanoparticles. *Adv. Mater.* **2013**, *25*, 3144–3176.

[17] Park, Y. I.; Kim, J. H.; Lee, K. T.; Jeon, K. S.; Na, H. B.; Yu, J. H.; Kim, H. M.; Lee, N.; Choi, S. H.; Baik, S. I. et al. Nonblinking and nonbleaching upconverting nanoparticles as an optical imaging nanoprobe and T_1 magnetic resonance imaging contrast agent. *Adv. Mater.* **2009**, *21*, 4467–4471.

[18] Grootveld, M.; Halliwell, B. Aromatic hydroxylation as a potential measure of hydroxyl-radical formation *in vivo*. Identification of hydroxylated derivatives of salicylate in human body fluids. *Biochem. J.* **1986**, *237*, 499–504.

[19] Jang, S. W.; Lopez-Anido, C.; MacArthur, R.; Svaren, J.; Inglese, J. Identification of drug modulators targeting gene-dosage disease CMT1A. *ACS Chem. Biol.* **2012**, *7*, 1205–1213.

[20] Li, D. L.; Zhao, X. B.; Zhang, L. W.; Li, F.; Ji, N.; Gao, Z. X.; Wang, J. S.; Kang, P.; Liu, Z. F.; Shi, J. Y. et al. ^{68}Ga-PRGD2 PET/CT in the evaluation of glioma: A prospective study. *Mol. Pharmaceutics* **2014**, *11*, 3923–3929.

[21] Betzer, O.; Shwartz, A.; Motiei, M.; Kazimirsky, G.; Gispan, I.; Damti, E.; Brodie, C.; Yadid, G.; Popovtzer, R. Nanoparticle-based CT imaging technique for longitudinal and quantitative stem cell tracking within the brain: Application in neuropsychiatric disorders. *ACS Nano* **2014**, *8*, 9274–9285.

[22] Sun, C.; Lee, J. S. H.; Zhang, M. Q. Magnetic nanoparticles in MR imaging and drug delivery. *Adv. Drug Deliv. Rev.* **2008**, *60*, 1252–1265.

[23] Mornet, S.; Vasseur, S.; Grasset, F.; Duguet, E. Magnetic nanoparticle design for medical diagnosis and therapy. *J. Mater. Chem.* **2004**, *14*, 2161–2175.

[24] Terreno, E.; Delli Castelli, D.; Viale, A.; Aime, S. Challenges for molecular magnetic resonance imaging. *Chem. Rev.* **2010**, *110*, 3019–3042.

[25] Tong, S.; Hou, S. J.; Zheng, Z. L.; Zhou, J.; Bao, G. Coating optimization of superparamagnetic iron oxide nanoparticles for high T_2 relaxivity. *Nano Lett.* **2010**, *10*, 4607–4613.

[26] Choi, J. S.; Lee, J. H.; Shin, T. H.; Song, H. T.; Kim, E. Y.; Cheon, J. Self-confirming "AND" logic nanoparticles for fault-free MRI. *J. Am. Chem. Soc.* **2010**, *132*, 11015–11017.

[27] Su, M. N.; Ye, J.; Li, Q. W.; Ge, W.; Zhang, Y. Y.; Jiang, H.; Amatore, C.; Wang, X. M. *In vivo* accurate target bio-marking of tumors through *in-situ* biosynthesized fluorescent zinc nanoclusters. *RSC Adv.* **2015**, *5*, 74844–74849.

[28] Trachootham, D.; Alexandre, J.; Huang, P. Targeting cancer cells by ROS-mediated mechanisms: A radical therapeutic approach? *Nat. Rev. Drug Discov.* **2009**, *8*, 579–591.

[29] Bienert, G. P.; Schjoerring, J. K.; Jahn, T. P. Membrane transport of hydrogen peroxide. *Biochim. Biophys. Acta* **2006**, *1758*, 994–1003.

[30] Wang, H. P.; Jiang, H.; Wang, X. M. Construction of strong alkaline microcavities for facile synthesis of fluorescence-tunable ZnO quantum dots. *Chem. Commun.* **2010**, *46*, 6900–6902.